Relating aerosol mass spectra to composition and nanostructure of soot particles

Malmborg, Vilhelm B.; Eriksson, Axel C.; Török, Sandra; Zhang, Yilong; Kling, Kirsten Inga; Martinsson, Johan; Fortner, Edward C.; Gren, Louise; Kook, Sanghoon; Onasch, Timothy B.

Total number of authors:
12

Published in:
Carbon

Link to article, DOI:
10.1016/j.carbon.2018.10.072

Publication date:
2019

Document Version
Publisher's PDF, also known as Version of record

Carbon 142 (2019) 535–546

Contents lists available at ScienceDirect

Carbon

journal homepage: www.elsevier.com/locate/carbon

Relating aerosol mass spectra to composition and nanostructure of soot particles

Vilhelm B. Malmborg [a, *], Axel C. Eriksson [a], Sandra Török [b], Yilong Zhang [c], Kirsten Kling [d, 1], Johan Martinsson [e, 2], Edward C. Fortner [f], Louise Gren [a], Sanghoon Kook [c], Timothy B. Onasch [f], Per-Erik Bengtsson [b], Joakim Pagels [a]

[a] Division of Ergonomics and Aerosol Technology, Lund University, Box 118, SE-22100, Lund, Sweden
[b] Division of Combustion Physics, Lund University, Box 118, SE-221 00, Lund, Sweden
[c] School of Mechanical and Manufacturing Engineering, University of New South Wales, Sydney, NSW, 2052, Australia
[d] National Research Centre for the Working Environment, 2100, Copenhagen, Denmark
[e] Division of Nuclear Physics, Lund University, Box 118, SE-221 00, Lund, Sweden
[f] Center for Aerosol and Cloud Chemistry, Aerodyne Research, Inc., 45 Manning Rd., Billerica, MA, 01821, USA

ARTICLE INFO

Article history:
Received 14 May 2018
Received in revised form
21 September 2018
Accepted 21 October 2018
Available online 22 October 2018

ABSTRACT

The composition and carbon nanostructure of soot are important parameters influencing health and climate effects, and the efficacy of soot mitigation technologies. We used laser-vaporization, electron-ionization aerosol mass spectrometry (or SP-AMS) to systematically investigate relationships between aerosol mass spectra, carbon nanostructure (HRTEM), and composition (thermal-optical carbon analysis) for soot with varying physicochemical properties. SP-AMS refractory black carbon concentrations (based on $C^+_{\leq 5}$ clusters) were correlated to elemental carbon ($r = 0.98$, $p < 10^{-8}$) and equivalent black carbon (aethalometer) concentrations. The SP-AMS large carbon ($C^+_{\geq 6}$, midcarbons and fullerene carbons) fraction was inversely correlated to fringe length ($r = -0.97$, $p = 0.028$) and linearly correlated to the fraction of refractory organic carbon that partially pyrolize during heating ($r = 0.89$, $p < 10^{-4}$). This refractory organic carbon material was incompletely detected with conventional aerosol mass spectrometry (flash vaporization at 600 °C). This suggests that (SP-AMS) refractory carbon cluster analysis provides insight to chemical bonding and nanostructures in refractory carbon materials, lowcarbons ($C^+_{\leq 5}$) indicate mature soot and large carbons indicate refractory organic carbon and amorphous nanostructures related to C_5-components. These results have implications for assessments of soot particle mixing state and brown carbon absorption in the atmosphere and enable novel, on-line analysis of engineered carbon nanomaterials and soot characteristics relevant for climate and health.

1. Introduction

Atmospheric soot particles form under incomplete combustion conditions in internal combustion engines, gas turbine engines (e.g., airplanes), wild and prescribed burns, and domestic wood-stoves [1–3]. Soot is an effective absorber of incoming solar radiation [4] and causes adverse health effects in humans [5–8]. As a result, soot is an important short-term climate forcer and a major contributor to air pollution [9,10]. Soot particles are generally composed of light absorbing refractory carbonaceous components often referred to as black carbon (BC) [11], ash, and condensed non-refractory semi-volatile and low volatility organic material [12]. Both fuel and combustion conditions strongly influence physical and chemical properties of soot. Soot can exhibit large variations in, for example, the carbon nanostructure [13,14], hydrogen to carbon ratio [15], surface functional groups [16], and condensed polycyclic aromatic hydrocarbons (PAHs) [15,17]. These variations in soot properties, in turn, influence the applications and strategies to mitigate soot emissions, climate forcing, and human health relevant aspects of the soot.

High-resolution transmission electron microscopy (HRTEM) has been widely applied to characterize the soot nanostructure

* Corresponding author.
E-mail address: vilhelm.malmborg@design.lth.se (V.B. Malmborg).
[1] Present address: Center for Electron Nanoscopy, Technical University of Denmark, Fysikvej 307, 2800 Kgs, Lyngby, Denmark.
[2] Present address: Medical Radiation Physics, Lund University, Box 118, SE-221 00, Lund, Sweden.

https://doi.org/10.1016/j.carbon.2018.10.072

[1,13,17–24]. It is found in HRTEM images that the refractory part of soot particles are composed of carbon layers, appearing as fringes, whose physical dimensions and organization reveal important information regarding the maturity and graphitization level of the particles [18,25,26]. Soot maturity is a qualitative description of the optical and physicochemical characteristics of soot. Soot maturity is commonly used to relate soot properties with time/position inside a flame, for example at increasing heights above the burner in premixed flames. As soot matures, the hydrogen to carbon ratio decreases [27,28] and the structural order of the carbon nanostructure and size of carbon lamellae have been found to increase [29,30]. Immature soot particles exhibit amorphous carbon nanostructures characterized by short and often highly curved fringes. Mature soot particles, in general, have a core-shell internal structure with short fringe segments forming amorphous core regions that are concentrically surrounded by a shell of longer and straighter carbon layers [31,32]. Characterization using HRTEM has revealed strong connections between the carbon nanostructure and reactivity towards oxidation [13,14,16,22,24,33]. This relationship can influence the ability to efficiently remove soot, for example in engine exhaust using diesel particulate filters. Mature soot with longer and straighter fringes (i.e., large and flat carbon layers) is less reactive towards oxidation. The reduced reactivity with increasing soot maturity is explained by reduced curvature (i.e., reduced tortuosity) and a relative decrease in the number of reactive edge-site atoms as the carbon layers grow in size [13,33]. Moreover, soot maturity and variations in composition and nanostructure influence the mass absorption cross section (MAC) [34] and absorption Angstrom exponent [11,35–38] which to a large extent determine the soot climate impact.

Soot formation mechanisms in different environments are intriguingly complex [17] and the different environments in which soot formation occur can result in vastly different soot properties. Although soot formation mechanisms have long remained elusive [39], the hydrogen-abstraction-C_2H_2-addition (HACA) mechanism [40,41] has been important in describing the formation and growth of aromatics and soot particles. The HACA framework identifies stabilomer sequences in order for aromatic growth reactions to become irreversible, a critical element also with respect to the growth of other forms of carbon such as fullerenes [40]. PAHs have long been recognized as soot precursor molecules [17,42] and incipient soot particles have been considered to form by the stacking of PAHs into three-dimensional structures [31,43]. Reilly et al. [44] identified a transition from PAHs to fullerenes in the first, very nascent, soot particles in a flame. Johnson et al. [45] identified the importance of low molecular weight (<400 u) PAHs with pentagonal ring systems and fullerene formation in the very early stages of formation of a carbon black soot (engineered soot nanoparticles). In the latter experiment, fullerenes and fullerenic nanostructures were incorporated into the soot matrix simultaneously with high molecular weight PAHs annealed into the soot shortly after soot formation. The fullerenes were incorporated into the soot but also destroyed upon further growth and oxidation [45]. More recently, Johansson et al. [46] provided strong evidence for soot formation occurring from resonance-stabilized C_5-containing radical species and clustering of hydrocarbons by radical-chain reactions (CHRCR). The CHRCR mechanism proceeds through both aromatic and aliphatic soot precursors and can explain the typical core-shell nanostructure of mature soot particles.

Particulate matter from low temperature combustion processes often contain refractory organic carbon not removed by heating to 300 °C–650 °C [35,47,48]. This group of compounds is challenging to characterize due to its low volatility and thermal degradation due to pyrolysis. In fact, on-line state of the art techniques such as combinations of BC absorption monitors and conventional aerosol mass spectrometry may not be capable of detecting this group of species [35,49]. Yet, due to its aromatic character and enhanced UV-VIS (brown carbon) absorption, soot containing these refractory organic carbon compounds may induce additional health and climate effects. Furthermore, there may be relationships and overlap between disordered materials constituting immature soot and refractory organic carbon (e.g., [50]). Therefore, there is a need to compare methods used in different disciplines to decipher diverse aspects of these materials and to validate novel in-situ techniques to classify these groups of compounds.

An aerosol mass spectrometer capable of detecting refractory carbon components is the soot particle aerosol mass spectrometer (SP-AMS) [51]. In the SP-AMS, aerosol particles are focused into high vacuum (10^{-7} mbar) by an aerodynamic lens. Infrared light absorbing particles, such as BC-containing particles, vaporize (in-flight) when the focused beam of aerosol particles passes through an intracavity Nd:YAG IR laser (1064 nm). The vapors are ionized using electron ionization (70 eV) and subsequently detected in a high-resolution time-of-flight mass spectrometer. Molecules fragment upon vaporization and ionization in the SP-AMS. The SP-AMS refractory black carbon (rBC) concentration is determined from the elemental carbon cluster fragments C^+_{1-5} (lowcarbons). Lowcarbon signal intensities are generally dominated by C^+_3 followed by C^+_1, and have been shown to correlate with optically determined equivalent BC concentrations for mature soots of different sources [51–53]. Some soots (select flame soots, carbon blacks and biomass combustion emissions) can produce SP-AMS mass spectra with significant ion signals at higher carbon numbers [51–55] in the range of C^+_{6-29} (midcarbons) and $C^+_{\geq 30}$ (fullerene carbons). These large carbons ($C^+_{\geq 6}$), observed for some soots in SP-AMS mass spectra, may have ring structures (midcarbons) and fullerene structures [52] due to the stability of these structures at large carbon numbers [56].

Both fullerenes and fullerenic soot nanostructures incorporate five membered aromatic rings (C_5). Formation of C_5-containing nanostructures have been suggested to proceed through partial oxidation of benzene to the phenoxy radical and subsequent CO loss, resulting in C_5 [18]. Laser heating (at 1064 nm and other) can result in annealing of the soot nanostructure [57,58]. The degree of annealing depends on laser power (or heating rate) [58] and the initial order of the soot nanostructure [59]. Annealing of graphitizable and non-graphitizable carbon materials results in different end structures. C_5 structures were recently identified as the cause of non-graphitizability in non-graphitizable chars [60]. Whether midcarbons and fullerene carbons are existing structures in the soot or form upon annealing in the SP-AMS laser interaction (for example from C_5-containing precursors) prior to its complete vaporization has not yet been verified. However, these large carbons have been hypothesized to relate to variations in the initial soot carbon nanostructure and immature soot properties [51–54]. This study presents the first attempt to test this hypothesis by benchmarking the on-line SP-AMS mass spectra analysis against off-line HRTEM analysis of the soot carbon nanostructure and off-line thermal-optical carbon (OC/EC) analysis of the soot composition. In this study, soot of varying maturity and diverse physicochemical properties were generated using a miniature combustion aerosol standard (miniCAST) soot generator. The results suggest strong relationships between the refractory carbon cluster (rC^+_x) distribution in SP-AMS mass spectra, the soot carbon nanostructure, and particle composition.

2. Method

2.1. Experimental overview

The experimental set-up to examine the relationship between the soot carbon nanostructure, thermal-optical carbon fractions, and refractory carbon cluster (rC_x^+) distributions in SP-AMS mass spectra is given in Fig. 1. The main set-up consisted of (a) a miniature combustion aerosol standard (miniCAST) soot generator (model 5201C; Jing ltd), (b) options to heat the aerosol in a thermodenuder (250 °C) and ceramic tube furnace (500 °C), (c) a dilution stage (approximate total dilution of 1:250), and (d) aerosol instruments. The set-up has previously been described in detail [35]. The mini-CAST was operated at five different operating points (OPs) 1, 3, 5, 6, and 7 by altering the flow of oxidation air and by mixing the fuel gas with a nitrogen (N_2) mixing flow (see Supplementary data and Table S1). For an increased OP number, an increased N_2 dilution and reduced oxidation air flow was used that reduces the adiabatic flame temperature. This reduces the rate of the in-flame evolution of soot properties before the miniCAST flame is quenched and results in the generation of soot with different physicochemical properties and soot with less mature character [35,47]. The dilution was accomplished through two ejector diluters (Dekati® Diluter DI-1000) in series and supplied with air at room temperature that passed a HEPA-filter and an activated carbon filter. In addition to the main set-up, a more detailed heating experiment was conducted on soot from a single miniCAST setting (OP5 using undiluted exhaust) by ramping the temperature of the ceramic tube furnace in steps from 25 °C to 925 °C.

The diluted miniCAST soot aerosol was analyzed on-line using a soot particle aerosol mass spectrometer (SP-AMS; Aerodyne Inc. Billerica, USA), a scanning mobility particle sizer (SMPS; Electrostatic Classifier model 3071 TSI Inc, CPC model 3775 TSI Inc), and a 7 wavelength aethalometer (Model: AE33; Magee Scientific Corp., Berkeley, USA). Untreated (bypass) and heat-treated (250 °C and 500 °C) miniCAST soot was also collected for off-line thermal-optical carbon analysis (i.e., OC/EC) and HRTEM analysis. The SP-AMS was used to probe the non-refractory organic aerosol (OA) and carbon clusters of refractory origin. In the experiments, positively charged carbon clusters were measured between mass-to-charge ratio (m/z) 12 and m/z 708 ($C_1^+ - C_{59}^+$) and divided in three classes: lowcarbons ($C_1^+ - C_5^+$), midcarbons ($C_6^+ - C_{29}^+$), and fullerene carbons ($C_{30}^+ - C_{59}^+$). Large carbons $C_{\geq 6}^+$ refer to the sum of midcarbons and fullerene carbons. The aethalometer provided real-time measurements of equivalent BC concentrations derived from light absorption at 880 nm and 950 nm. Mass estimations from SMPS size distributions were derived as previously described in Török et al. [35]. The off-line thermal-optical carbon analysis was used to quantify the operationally defined organic carbon ($OC_{1\text{-}4}$), elemental carbon (EC), pyrolytic carbon (PC), and total carbon (TC) mass according to the Eusaar_2 protocol [61]. We use the standard definition for OC referring to the sum of $OC_{1\text{-}4}$ and PC. $OC_{1\text{-}4}$ were evaluated in inert He and EC in He mixed with 2% O_2. PC was determined from the thermograms and subtracted from the EC concentration. Increased light absorption may occur during the evaluation of $OC_{1\text{-}4}$. PC mass is then defined by the material removed in the He mixed with 2% O_2 evaluation of EC until reaching the initial light absorption. Further information on the OC/EC analysis is included in the Supplementary data. Information on the carbon nanostructure of the soot particles (fringe lengths and tortuosity, median and lognormal parameters) was derived from the HRTEM analysis and using image post-processing [62] previously used to characterize soot nanostructure [63–66]. A detailed description of the HRTEM analysis including a flowchart (Fig. S1) can be found in the Supplementary data.

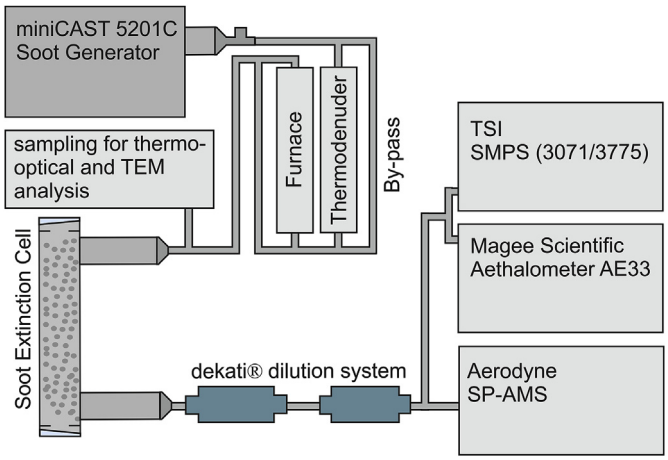

Fig. 1. Experimental set-up. The set-up included the soot extinction cell but is not part of the current analysis. Results on optical properties including the soot extinction cell have been published previously [35]. (A colour version of this figure can be viewed online.)

2.2. Description of the SP-AMS set-up, calibration, and tuning

The SP-AMS [51] incorporates an infrared Nd:YAG ($\lambda = 1064$ nm) intracavity laser into the Aerodyne aerosol mass spectrometer (AMS) [67]. The intracavity laser enables vaporization of highly refractory light absorbing (at $\lambda = 1064$ nm) particles, in particular refractory black carbon (rBC) components. The SP-AMS can be operated with the laser vaporizer on or off, while the tungsten vaporizer (~600 °C), which vaporizes non-refractory components, is always heated. The vaporization is followed by electron ionization (70 eV) of the vapors and detection of positively charged ions in a high resolution time-of-flight mass spectrometer. The mass spectrometer was set-up to record positive ions in the range m/z ~10–710.

Mass calibration of non-refractory components was performed according to the standard procedure using 300 nm (mobility diameter) ammonium nitrate particles. The non-refractory organic aerosol (OA) include PAHs and was evaluated in the conventional AMS mode (SP-AMS laser off) and was assigned the default relative ionization efficiency (RIE) of 1.4 (relative to NO_3). SP-AMS (laser on) mass calibration of refractory black carbon (rBC) was performed using 300 nm carbon black particles (Regal Black; Cabot Inc., Boston, MA, USA) and lowcarbon ($C_{\leq 5}^+$) intensities. The relative ionization efficiency of rBC to NO_3 (RIE_{RB}) was determined to 0.29. Non-refractory OA ($C_xH_y^+$ and $C_xH_yO_z^+$ in the range m/z 10 to ~ m/z 120 and PAHs in the range m/z 202–300), lowcarbons ($C_{\leq 5}^+$), and midcarbons (C_{6-29}^+) were derived from curve-fitting with high-resolution data in the PIKA analysis module (version 1.15D). Signal intensities from fullerene carbons ($C_{\geq 30}^+$) were derived by integrating the SP-AMS signal at unit-mass resolution. Information on the SP-AMS quantification of PAHs and separation of midcarbon and PAH ions at the same nominal m/z is found in the Supplementary data.

The influence of laser power on large carbons was evaluated by performing a laser intensity sweep on heat-treated (250 °C) miniCAST OP6 soot (section 3.1.2). The reported laser powers are the measured laser bleed-through of the output coupler mirror. We monitored laser power (mW) with an OPHIR power monitor and laser intensity (W/m^2) with a CCD-camera. The camera laser intensity was calibrated against the power monitor. In this

evaluation, the SP-AMS was set-up to record mass spectra including positively charged carbon cluster ions up to $C^+_{>200}$ (m/z 10–2500). Above m/z 700, C^+_{60} (m/z 720) and C^+_{70} (m/z 840) were identified as two additionally strong fullerene carbon signals. However, including larger carbon clusters above m/z 700 did not significantly influence the ratio of large carbons to rC^+_x (the intensity ratio of large carbons to the total refractory carbon clusters).

The tuning of the voltages in the SP-AMS mass spectrometer influenced the distribution of large carbons. Specifically, altering the tuning of the ion extractor between negative and positive voltages, with all other parameters constant, would significantly change the rC^+_x mass spectrum. Different tunings could maximize or minimize large carbon cluster ion signals in a given SP-AMS rC^+_x mass spectrum for soot particles that exhibited large carbon ion signals; changing tunings did not result in large carbon ion signals being observed for mature soot types. Thus, the results and conclusions presented here are not dependent upon the SP-AMS tuning, only the magnitude of the observed large carbon ion signals. A thorough investigation of SP-AMS factors influencing the detection of large carbons in the SP-AMS will be published elsewhere. Our current understanding advocates a tuning of voltages which optimizes large carbon ion signals and allows simultaneous and reproducible detection of lowcarbons, midcarbons, and fullerene carbons.

The OPs 5, 6, and 7 were all associated with strong signals from mid- and fullerene carbons. To estimate the mass concentrations of the material responsible for these large carbon signals, knowledge of their relative ionization efficiencies is crucial. The SP-AMS relative ionization efficiency for large carbons is currently unknown. If large carbons were associated with non-refractory aliphatic or aromatic hydrocarbons we would expect these ions to have relative ionization efficiencies similar to OA (RIE_{OA} larger than 1). OA has traditionally been assigned a relative ionization efficiency of 1.4. Recent evaluations suggest an RIE_{OA} of 1.6 (±0.3) for OA with carbon oxidation states commonly observed in ambient OA, and even higher RIE for reduced organic species [68]. Since large carbons appear to have originated from refractory components we have treated them as having the same relative ionization efficiency with respect to NO_3 as lowcarbons, hence their concentrations are given as Regal Black equivalent mass concentration ($RIE_{RB} = 0.29$).

3. Results and discussion

3.1. SP-AMS analysis

3.1.1. Refractory carbon cluster (rC^+_x) analysis

Refractory carbon cluster (rC^+_x) distributions in SP-AMS mass spectra were notably different between the miniCAST operating points (OP). Fig. 2 shows the mass spectra of rC^+_x from OP 3, 5, 6, and 7. A higher OP represents an increased N_2 dilution of the miniCAST propane fuel flow and reduced oxidation air flow rate, and thus reduced adiabatic flame temperatures. The mass spectrum from OP1 was similar to that of OP3 and is not shown. Lowcarbons (C^+_1-C^+_5 with m/z 12–60) dominated the mass spectra of OP1 and OP3, while OPs 5, 6, and 7 showed increasing fractions of large carbons ($C^+_{\geq 6}$, $m/z \geq 72$) with increasing N_2 fuel dilution. The large carbons consisted of midcarbons (C^+_6-C^+_{29}, m/z 72–348) separated by 12 Da and fullerene carbons (C^+_{30}-C^+_{59}, m/z 360–708) of mainly even carbon numbers separated by 24 Da.

Among individual large carbons, the strongest midcarbon cluster was C^+_{11} (m/z 132) followed by C^+_{10}, C^+_{15}, C^+_7 and C^+_{14} (m/z 120, 180, 84, and 168). These carbon clusters contributed more than 10% each and their sum contributed more than two thirds of the total midcarbon signal. The strongest fullerene ions were C^+_{36} (m/z 432), C^+_{44} (m/z 528), and C^+_{50} (m/z 600). The distributions of mid- and fullerene carbon cluster ions were similar between OPs 5, 6, and 7, although large carbon intensities increased relative to low carbons with increasing miniCAST OP.

3.1.2. Laser power influence on SP-AMS refractory C^+_x mass spectra

Fig. 3 shows the laser power influence on signals from individual carbon clusters (Fig. 3a) and the total carbon ion signal when grouped into low-, mid-, and fullerene carbons (Fig. 3b). C^+_3 and lowcarbons, the most commonly used proxies for rBC, were approximately doubled by a threefold increase in laser power. Fig. 3a shows that the fullerene carbon cluster C^+_{60} had a slightly elevated response to laser power compared to C^+_3. However, Fig. 3b shows that, when grouped, fullerene carbons (C^+_{30-59}) had a similar response to laser power as did lowcarbons (C^+_{1-5}). The midcarbon cluster ions (C^+_{6-29}) appeared to fragment more strongly with higher laser power than did lowcarbons or fullerene carbons (Fig. 3b). The midcarbons appeared to preferentially fragment into C^+_1. This preferential path for fragmentation of midcarbons resulted in C^+_1 to C^+_3 ratios greater than 1 at high laser powers (>15 mW in Fig. 3). Hence, high laser power and fragmentation of midcarbons may explain previous SP-AMS observations related to high C^+_1 to C^+_3 ratios and the simultaneous observation of large carbons [54]. This effect could potentially induce bias to the determination of especially low- and midcarbons when comparing instrument to instrument.

Thermal ionization of large carbons has been shown to occur in the SP-AMS laser vaporization at high laser fluences [52]. In addition, dissociation of C^+_{60} (i.e., the expulsion of C_2 and other C_x clusters) may occur at similar energies to thermal ionization [69,70] and influence rC^+_x distributions. Thermal ionization in the SP-AMS was shown to be of importance primarily for very large carbons ($C^+_{>70}$) [52]. The increased sensitivity to C^+_{60} compared to C^+_3 with increasing laser power suggests a contribution from thermal ionization for this ion at the highest laser fluencies. However, such a dependence was not seen for the full class of fullerene carbons in Fig. 3b. Thus our analysis shows that during the current experiments, laser induced thermal ionization and power dependent fragmentation had only a very minor impact on the carbon cluster distributions.

3.1.3. Non-refractory OA and rC^+_x after heat-treatment to 250 °C and 500 °C

Fig. 4a shows the ratio of non-refractory organic aerosol (OA_{AMS}), including PAHs, derived in conventional AMS mode (laser off) to the total carbon mass (TC) derived from thermal-optical carbon analysis. Fig. 4b shows OA_{AMS} to PAH_{AMS} ratios. The ratios are shown for untreated soot (BP), after heating to 250 °C in the thermodenuder, and after heating to 500 °C in the ceramic furnace.

MiniCAST OPs 1, 3 and 5 generated particles with low non-refractory OA_{AMS} content (Fig. 4a, BP). Non-refractory OA_{AMS} increased for OP6 and OP7 but remained low with respect to TC (OA_{AMS} to TC ratios of 0.05 and 0.06 respectively). Approximately half of the OA_{AMS} signal at OP6 and OP7 was attributed to PAHs (Fig. 4b). In the soot from miniCAST OP1 and OP3, four-membered PAHs at m/z 202 dominated the total particulate PAH mass (not shown). The mass fraction of PAHs at m/z 202 was low at OPs 5, 6, and 7, where larger 4, 5 and 6 membered PAHs (m/z 226–300) dominated the particle PAH mass. Heating the aerosol in the thermodenuder (250 °C) and ceramic furnace (500 °C) removed approximately 30% of the non-refractory OA_{AMS} for OP7 (Fig. 4a) and up to 60% for OP6. Heating the aerosol in the ceramic furnace to 500 °C resulted in an almost complete evaporation of PAHs (PAH_{AMS} to OA_{AMS} ratios less than 0.15). OA to TC ratios will be further discussed in Fig. 6 (section 3.2).

Large carbon to rC^+_x ratios and midcarbons and fullerene carbons to rC^+_x ratios are shown in Fig. 5a and b, respectively, for

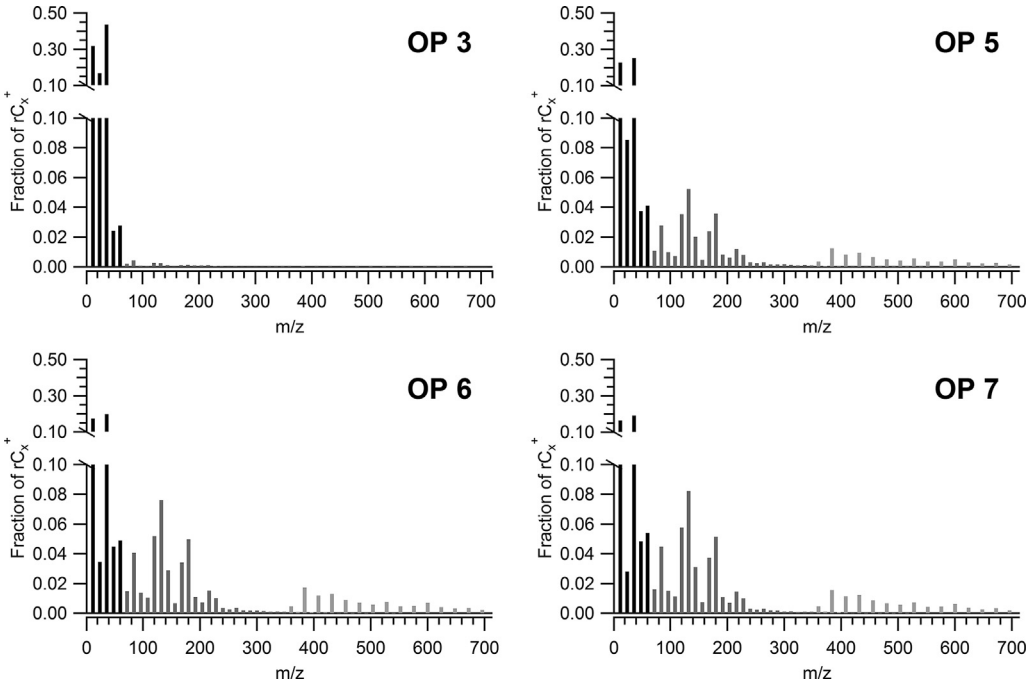

Fig. 2. SP-AMS normalized refractory carbon cluster (rC_x^+) distributions for soot from miniCAST OP 3, 5, 6 and 7. Lowcarbons (C_1^+-C_5^+ with m/z 12–60), midcarbons (C_6^+-C_{29}^+, m/z 72–348), fullerene carbons (C_{30}^+-C_{59}^+, m/z 360–708). Larger carbon clusters ($C_{\geq 6}^+$, $m/z \geq 72$) increased relative to lowcarbon clusters (C_1^+-C_5^+, m/z 12–60) with increasing OP.

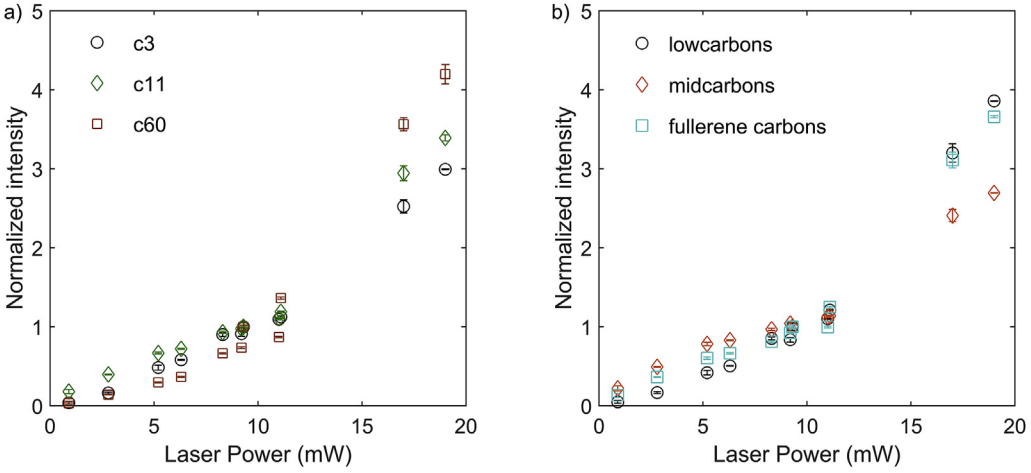

Fig. 3. SP-AMS laser intensity sweep on thermodenuded (250 °C) soot from mini-CAST OP6 and a) recorded C_3^+, C_{11}^+, and C_{60}^+ signals and b) recorded lowcarbon, midcarbon and fullerene carbon ion signals normalized to 9.3 mW laser power (i.e., signal is exactly 1 for 9.3 mW) and corrected for fluctuations in the miniCAST output concentration using equivalent BC (aethalometer). Laser power was recorded with an OPHIR laser power monitor from the bleed-through of the SP-AMS output coupler mirror. (A colour version of this figure can be viewed online.)

bypass (BP, 25 °C) and after heating to 250 °C in the thermodenuder and 500 °C in the ceramic furnace. Heating the soot to 250 °C had only minor influences on lowcarbons and midcarbons. Fullerene carbons increased slightly, which resulted in marginally higher large carbon to rC_x^+ ratios after heating to 250 °C. Further heating to 500 °C showed a moderate but significant decrease of midcarbons which resulted in lower large carbon to rC_x^+ ratios. Heating to 500 °C resulted in a minor decrease of the fullerene to rC_x^+ ratio for OP5, but did not influence this ratio in soot from OPs 6 and 7.

When comparing the SP-AMS laser-on mode and laser-off mode mass spectra, increases of fragments originating from aromatic or highly unsaturated aliphatic compounds ($C_xH_{y<x}^+$) were observed especially for higher miniCAST operating point (not shown). A strong contribution of $C_xH_{y<x}^+$ fragments to OA mass spectra has previously been found in SP-AMS laser-on mode for immature diesel soot [53], and can thus be related to increased H:C ratios in immature soots [31]. Additionally, CO, CO_2 and C_3O_2 increased for laser on (not shown). The relative abundance of these carbon and oxygen containing ions decreased with OP (increased N_2 fuel dilution) which likely reflects a less oxidized surface of the refractory material. However, the major difference in total soot aerosol mass spectra between the SP-AMS laser-on mode and laser-off mode were the refractory low-, mid- and fullerene carbon cluster ions (i.e., rC_x^+).

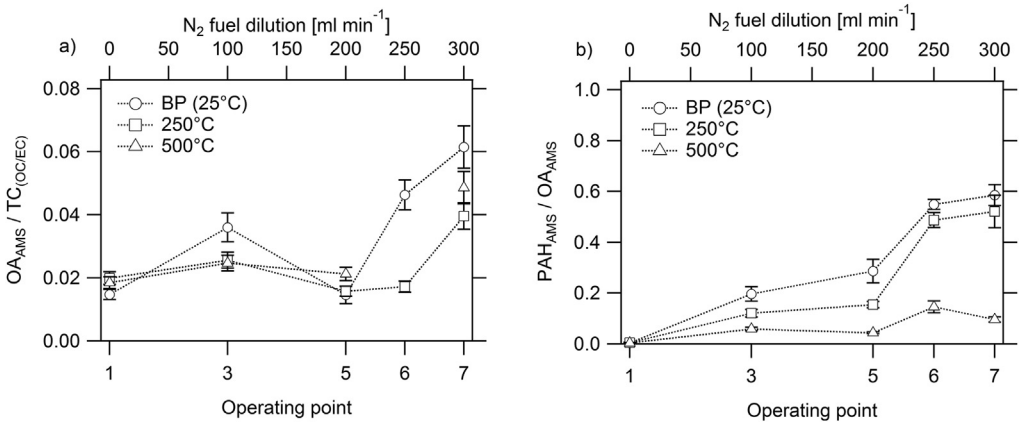

Fig. 4. a) Non-refractory organic aerosol (OA_{AMS}, including PAHs) to total carbon mass (TC) ratios and b) polycyclic aromatic hydrocarbon (PAH_{AMS}) to OA_{AMS} ratios for bypassing thermodenuder and furnace (BP), soot heated to 250 °C in a thermodenuder, and 500 °C in a ceramic furnace.

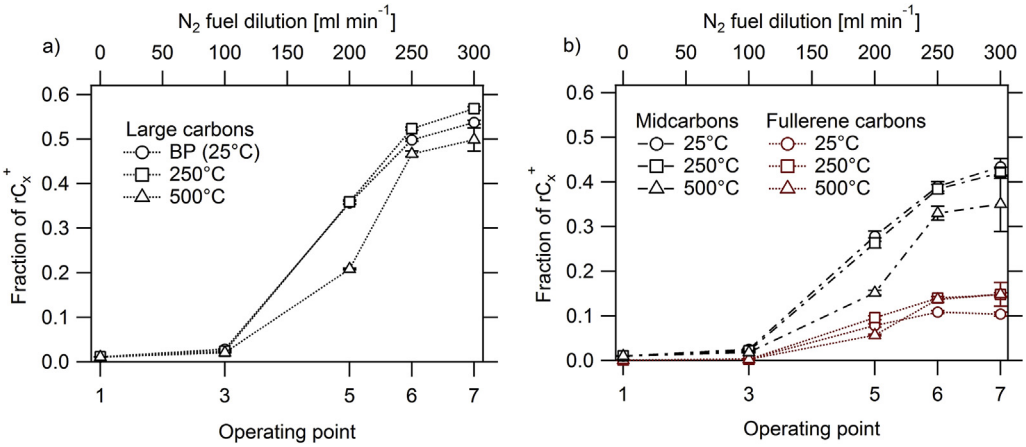

Fig. 5. SP-AMS a) total large carbon to rC_x^+ ratio and b) midcarbon to rC_x^+ and fullerene carbon to rC_x^+ ratio. (A colour version of this figure can be viewed online.)

In summary, Figs. 4 and 5 shows that heating the aerosol to 250 °C resulted in partial removal of non-refractory OA_{AMS} and a minor increase of fullerene carbons. Increased temperature to 500 °C further reduced the non-refractory particle fraction and resulted in reduced midcarbon signal intensity. These results suggest that there existed no strong relationship between non-refractory OA (including PAHs) and the large carbons (i.e., midcarbons and fullerene carbons were not formed from material related to non-refractory OA on soot heated to 250 °C nor 500 °C). Thus, the origin of the observed large carbons appear to be more refractory than typical organic compounds, but less refractory than elemental carbon or graphitic carbon which are related to both SP-AMS lowcarbons and equivalent BC (aethalometer).

3.2. Relationship between SP-AMS mass spectra and thermal-optical carbon analysis

The SP-AMS lowcarbon intensity was linearly correlated to both the elemental carbon (EC) mass and the equivalent BC (aethalometer) concentration (Supplementary data, Fig. S2) when including data from all OPs. This supports the use of the lowcarbon ($C_1^+ - C_5^+$) signal to derive refractory black carbon (rBC) mass concentrations from SP-AMS data, as has previously been suggested [52].

Table 1 shows the thermal-optical carbon analysis for the untreated (25 °C) miniCAST soot (for heat-treated samples, see Table S3 in Supplementary data). For soot from miniCAST OPs 1 and 3, EC dominated the total carbon (TC) mass while $OC_{1\text{-}4}$ were low (<5% of TC) and negligible amounts of pyrolytic carbon (PC) were formed upon heating. For the miniCAST OPs 5, 6, and 7, OC (the sum of $OC_{1\text{-}4}$ and PC) fractions increased with increasing OP up to more than 50% of the TC mass for OP 6 and 7.

Fig. 6 presents trends of the contribution to the total carbon mass (TC) from OC (sum of $OC_{1\text{-}4}$ + PC), non-refractory OA_{AMS}, and the sum of non-refractory OA_{AMS} and large carbon ($C_{\geq 6}^+$) concentration (RIE_{RB} equivalent). Comparing the OA_{AMS} to TC ratios and the OC to TC ratios in Fig. 6, OA_{AMS} (i.e., laser off) appears to represent OC for OPs 1 and 3, but only represent a small fraction of OC for OPs 5, 6, and 7. Including both OA_{AMS} and $C_{\geq 6}^+$ strongly improved the agreement with OC/TC ratios for all OPs, with a fairly strong and significant correlation ($r = 0.89$, $p < 10^{-4}$). The comparison in Fig. 6 is qualitative, as the RIE of the refractory material generating large carbons requires further evaluation, yet informative, and illustrates a strong correlation and a possible linear relationship between SP-AMS refractory large carbons and refractory OC (including PC).

In addition to Fig. 6, Fig. S3 (supplementary data) compares the non-refractory OA_{AMS} mass and OC (including PC) mass while Fig. S4 compares the sum of non-refractory OA_{AMS} and large carbon (RIE_{RB} equivalent) concentration versus OC mass. Including both non-refractory OA_{AMS} and large carbons significantly improved the correlation and reduced the difference in derived concentrations

Table 1
Thermal-optical carbon (OC/EC) analysis evaluated according to the EUSAAR_2 protocol for untreated (25 °C) miniCAST soot. Evaluations for the heat-treated (250 °C and 500 °C) are shown in the Supplementary data (Table S3). Carbon mass is divided into: organic carbon classes ($OC_{1\text{-}4}$) evaluated in inert He gas; elemental carbon (EC) evaluated in He gas mixed with 2% O_2; pyrolytic carbon (PC) defined from increased light absorption from refractory material during the evaluation of OC and removed first in the He mixed with 2% O_2 evaluation of EC.

MiniCAST operating point	N_2 dilution (l/min)	OC1	OC2	OC3	OC4	PC	EC
1	0	2.7%	1.3%	3.3%	2.0%	0.0%	90.7%
3	0.100	2.8%	0.5%	1.3%	0.2%	0.0%	95.2%
5	0.200	3.1%	1.3%	4.7%	3.5%	5.1%	82.4%
6	0.250	4.1%	3.7%	11.8%	12.9%	26.9%	40.6%
7	0.300	14.2%	10.0%	13.2%	15.3%	34.2%	13.2%

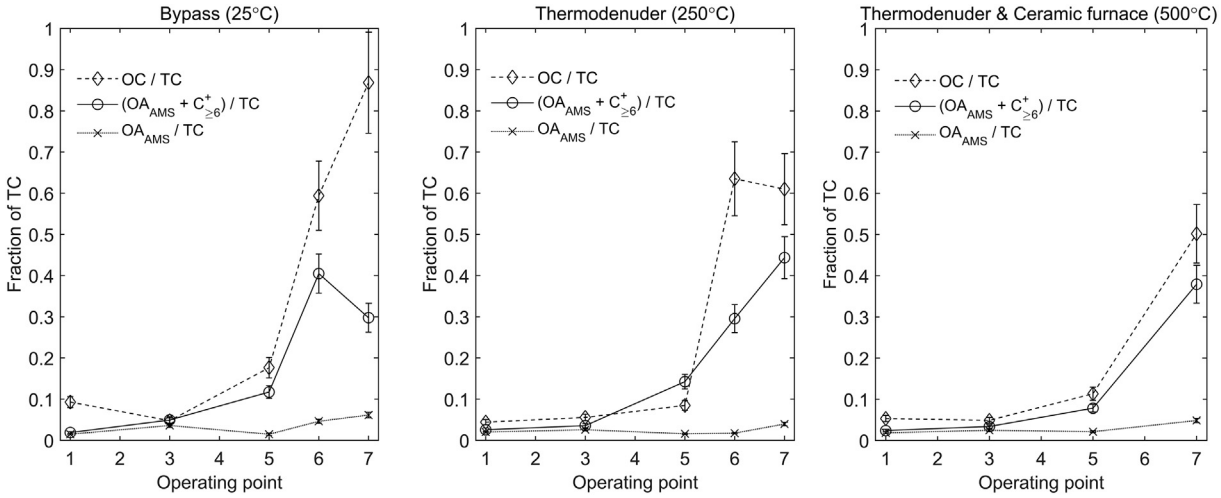

Fig. 6. OC ($OC_{1\text{-}4}$ + PC) to TC ratio, conventional AMS (SP-AMS laser off) OA_{AMS} to TC ratio, and the sum of OA_{AMS} and RIE_{RB} equivalent large carbon ($C^+_{\geq 6}$) to TC ratio after no heating (25 °C), after heating to 250 °C in the thermodenuder, and after heating to 500 °C in the ceramic furnace. OP6 at 500 °C was not included due to a measurement error.

between the SP-AMS and thermal-optical carbon analysis (see Fig. S3 and Fig. S4). The reported OA_{AMS} includes mass contribution from hydrogen and other heteroatoms. We have not attempted to remove this contribution for comparison with OC. For these flame soots this would only result in minor adjustments of the ratios and was neglected in this simplified comparison.

From these results, we hypothesize that refractory large carbons ($C^+_{\geq 6}$) derive mainly from material quantified as OC3, OC4, and PC in the thermal-optical carbon analysis. However, we anticipate that the classification of these components according to $OC_{1\text{-}4}$, PC, and EC may depend on several factors (e.g., sampled mass on filters, relative carbon mass from semi-volatile organic components, analysis protocol, compound molecular weight, etc.) and the observations in this study may not be generalized to all soot samples. We therefore expect that components giving rise to the large carbon signal can be evaluated in OC3, OC4, and PC, but also in EC1 and EC2 depending on the conditions.

The organic carbon classes ($OC_{1\text{-}4}$ and PC) in thermal-optical carbon analysis are related to the volatility of organic compounds. A higher OC class is synonymous to compounds of lower volatility. PC represents the least volatile organic carbon fraction [71]. In the EUSAAR_2 protocol, OC3 is evaluated at 450 °C and OC4 is evaluated at 650 °C in He. PC only evaporates (oxidizes) during the evaluation of EC in 2% O_2. Components that pyrolyze upon heating to 450 °C and 650 °C in He may be forming similar pyrolysis products on the AMS tungsten vaporizer (when used in the conventional AMS mode with the SP-AMS laser off). It can therefore be expected that soot from these higher miniCAST OPs include material classified as $OC_{1\text{-}4}$ and PC that cannot be vaporized on timescales and temperatures associated with the AMS flash vaporization (~5 s, 600 °C, and high vacuum) [72].

3.3. Soot nanostructure analysis by HRTEM and relation to SP-AMS mass spectra

High resolution images of the carbon nanostructure were obtained by high-resolution transmission electron microscopy (HRTEM). Fig. 7 shows HRTEM images of representative soot particles from the miniCAST OPs 3, 5, 6 and 7. SMPS particle size distributions show soot particle size decreasing from approximately 300 nm–80 nm when changing from OP3 to 7 [35]. In Fig. 7, a prominent change in the physical appearance of soot particles is apparent with increased miniCAST OP (increased N_2 flow, reduced oxidation air flow, and altered flame characteristics).

To analyze the carbon nanostructure, semi-automated image processing of carbon fringe length and tortuosity was conducted on images of non-overlapping parts of soot particles from miniCAST OPs 3, 5, 6, and 7. Fringe lengths decreased strongly with higher miniCAST OP (Table 2). The geometric mean fringe lengths (l_g) decreased from 0.61 nm to 0.51 nm for OP3 to OP7, the fringe length distributions became narrower (decreased geometric standard deviation, σ_l), and the proportion of fringes larger than 1 nm decreased for higher OP. In contrast, the curvature of the fringes (their tortuosity) increased with higher operating point. The geometric mean fringe tortuosity (τ_g) increased from 1.18 at OP3 to 1.23 at OP7.

The shorter fringe lengths and increased tortuosity with increasing OP indicate a change from more graphitized (more

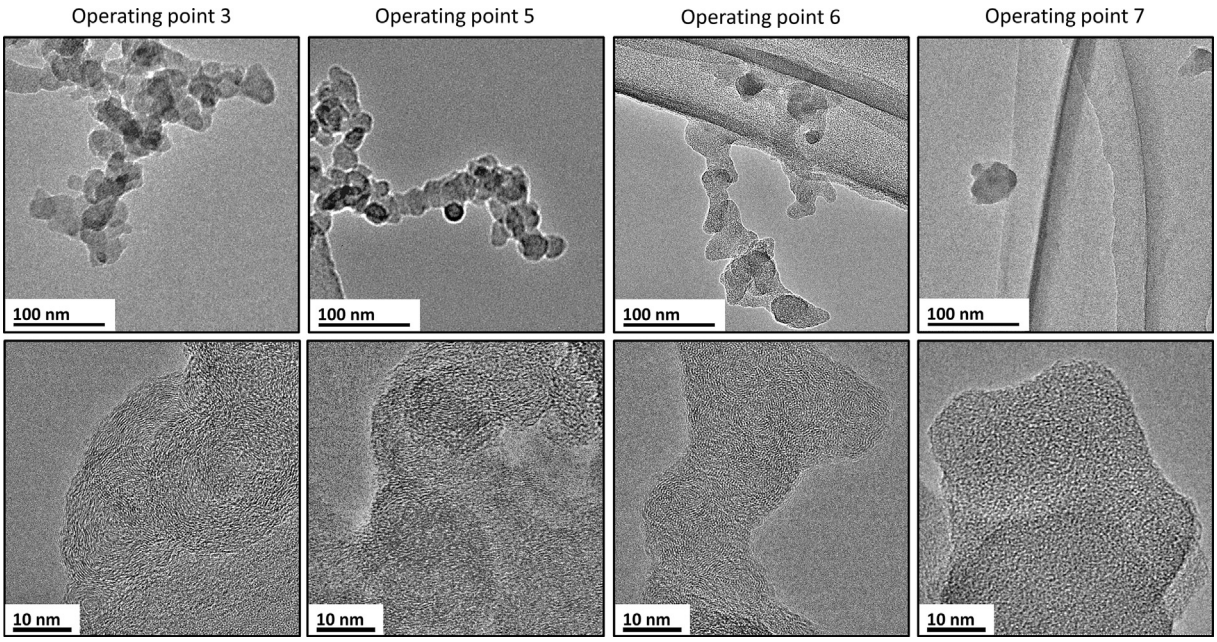

Fig. 7. Images from high-resolution transmission electron microscopy (HRTEM) of representative miniCAST soot particles (top) and soot carbon nanostructure (bottom).

Table 2
HRTEM analysis of the miniCAST soot nanostructure. Derived parameters for fringe length (l) and tortuosity (τ): median (l_m, τ_m), geometric mean (l_g, τ_g), geometric standard deviation (σ_l, σ_τ), and the fraction of measured fringes larger than 1 nm. Confidence intervals (95%) are shown in parentheses.

MiniCAST Operating point	N_2 dilution of fuel (l/min)	Fringe length			Fringe tortuosity			Fraction of total fringes >1 nm	Number of analyzed fringes (n)
		l_m	l_g	σ_l	τ_m	τ_g	σ_τ		
3	0.100	0.56 (±0.02)	0.61 (±0.02)	0.611 (±0.02)	1.13	1.18 (±0.01)	0.168 (±0.005)	35%	2387
5	0.200	0.52 (±0.01)	0.56 (±0.01)	0.566 (±0.01)	1.15	1.20 (±0.01)	0.165 (±0.004)	25%	3388
6	0.250	0.50 (±0.02)	0.54 (±0.02)	0.529 (±0.02)	1.15	1.21 (±0.01)	0.166 (±0.008)	21%	839
7	0.300	0.47 (±0.01)	0.51 (±0.01)	0.499 (±0.01)	1.18	1.23 (±0.01)	0.155 (±0.003)	15%	4019

mature), to less graphitized (less mature) soot. C_5 species in carbon lamellae introduce curvature (tortuosity) in the soot nanostructure [26,33,73] and prevents the stacking of parallel layers [74,75], resulting in amorphous soot nanostructures. The decrease in fringe length and increase in tortuosity is a result of decreasing adiabatic flame temperatures and altered flame characteristics with increasing miniCAST OP. Similar relationships between combustion temperatures and soot nanostructures have been found in, for example, diesel engines. High curvature structures have been linked to reduced combustion temperatures in diesel engines applying exhaust gas recirculation [76] and fringe lengths of in-cylinder soot have been shown to increase from the early to late combustion phase [77] and engine out [23]. The mean fringe length derived for OP3 is comparable to the fringe lengths observed in diesel engine exhaust soot during combustion with a fatty acid methyl ester [13]. The more amorphous soot from OP6 and OP7 have mean fringe lengths more similar to soot from a wildfire [73].

Fig. 8 shows the geometric mean fringe length (left axis, note the reversed scale), the large carbon to rC_x^+ ratio (right axis) and sum of $OC_{3\text{-}4}$ and PC to TC ratio (right axis) for OP 3, 5, 6, and 7. The large carbon to rC_x^+ ratio was negatively correlated to the geometric mean fringe length (Pearson correlation $r = -0.97$; $p = 0.028$), and positively correlated to the mean fringe tortuosity ($r = 0.92$; $p = 0.079$). These correlations suggest a strong relationship between the SP-AMS carbon cluster distribution and the soot nanostructure. A similar correlation was also found between the average fringe lengths and the $OC_{3\text{-}4}$ and PC to TC ratio ($r = -0.93$ and $p = 0.066$).

Fullerenes have C_5 rings incorporated into their structure. The SP-AMS detection of fullerene carbons can thus be a result of C_5-containing components present in the short carbon lamellae. While graphitic (C_6-containing) soot nanostructures almost exclusively fragment to lowcarbons, C_5-containing carbon lamellae may fragment into larger, and energetically favorable, fullerene structures. Midcarbons were exclusively detected simultaneously with fullerene carbons, making it plausible that they form from similar principles as fullerene carbons in the SP-AMS. Hence, the correlation between large carbons in SP-AMS soot mass spectra and shorter fringe lengths (and increased tortuosity) can represent an increased amount of C_5-containing species incorporated into the soot nanostructure. As a result, changes in the SP-AMS rC_x^+ distribution may possibly provide a real-time measurement of key parameters controlling soot reactivity.

3.4. SP-AMS measured refractory BC during evaporation and oxidation

The relative intensities of low-, mid-, and fullerene carbons changed upon heat treating the soot (Fig. 5). In addition to the

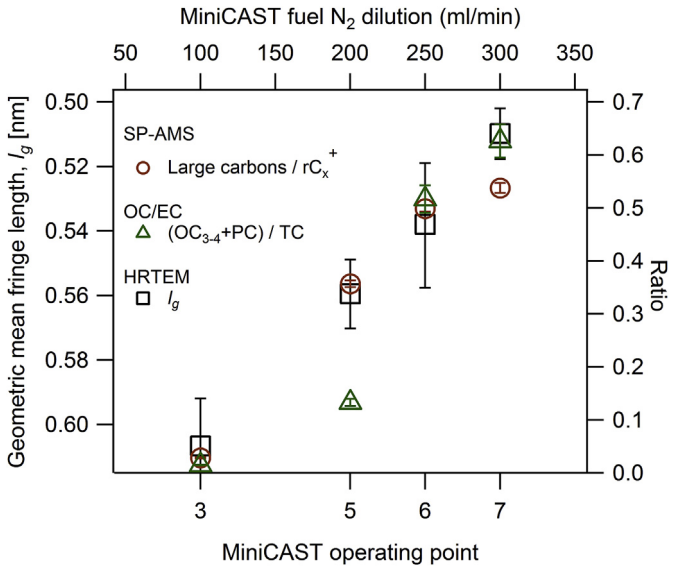

Fig. 8. Geometric mean fringe lengths (l_g) (left axis, note the reversed scale), large carbon to rC_x^+ ratios (right axis), and $OC_{3\text{-}4}$+PC to TC ratios (right axis) for the untreated soot from miniCAST OPs 3, 5, 6, and 7. Error bars represent (95%) confidence intervals for average fringe lengths and large carbon to rC_x^+ ratios, and estimated errors for the OC/EC analysis. The average fringe length was inversely correlated to the large carbon to rC_x^+ ratio ($r = -0.97$, $p = 0.028$) and sum of $OC_{3\text{-}4}$ and PC to TC ratio ($r = -0.93$, $p = 0.066$). (A colour version of this figure can be viewed online.)

bypass and thermodenuder experiments, a more detailed heating study where miniCAST OP5 soot was heated in small steps up to 925 °C in the ceramic tube furnace was carried out. Fig. 9 shows the evolution with temperature of SMPS derived mass, equivalent BC (aethalometer), and SP-AMS lowcarbons, midcarbons, fullerene carbons. The evolution of particle size distribution (electrical mobility) during the heating experiment is available in Supplementary data (Fig. S5). A general decrease in concentrations was observed with increasing temperature in the range 25 °C–250 °C and may partly be explained by evaporation of volatile material, but mainly due to increased thermophoretic losses in the cooling section after the thermodenuder. Fullerene carbons initially increased relative to low- and midcarbons when the soot was heated to between 150 °C – 400 °C. At higher temperatures (400 °C – 600 °C), midcarbons and fullerene carbons decreased rapidly relative to lowcarbons. The equivalent BC concentration, SMPS derived mass, and the SP-AMS lowcarbon concentration all decreased sharply at temperatures higher than 625 °C, at similar temperatures to the oxidation onset of mature diesel soot [78]. The equivalent BC and lowcarbon soot components were almost completely oxidized at 925 °C.

The evaporation/oxidation experiment shows that lowcarbons and equivalent BC were associated with the same material. Particle components from which the midcarbons and fullerenes originated were removed at temperatures approximately 200 °C lower than components associated with lowcarbons and equivalent BC. The particle mass derived from mobility measurements with the SMPS was largely unaffected between 400 °C–625 °C. This suggest that mobility sizes were insignificantly affected by mass loss from components associated with SP-AMS large carbons. Hence, the loss of large carbon associated material may have been related to internal oxidation patterns similar to those observed for some diesel engine soot at reduced combustion temperatures [14]. Alternatively, the loss of large carbon associated material may have been related to the pyrolysis of such components and a complete restructuring to refractory BC material. An increase of lowcarbons was not observed simultaneously to the decrease of large carbons, strengthening the hypothesis that the large carbon associated material was oxidized/evaporated rather than pyrolyzed.

3.5. SP-AMS rC_x^+ analysis and Raman spectroscopy

Changes in the nanostructure upon heating of soot from a miniCAST soot generator (model 5201C; Jing ltd) were previously studied using Raman spectroscopy by Ess et al. [79]. We identified similarities in the behavior of our SP-AMS lowcarbon to rC_x^+ ratio (the complement ratio to the large carbon to rC_x^+ ratio) and their Raman spectroscopy ID/IG ratio analysis. Changes in the soot nanostructure were studied upon heating (in air) by evaluating the ratio between the intensity of the D peak to the intensity of the G peak (ID/IG) in Raman spectra [79]. The ID/IG ratio is related to the

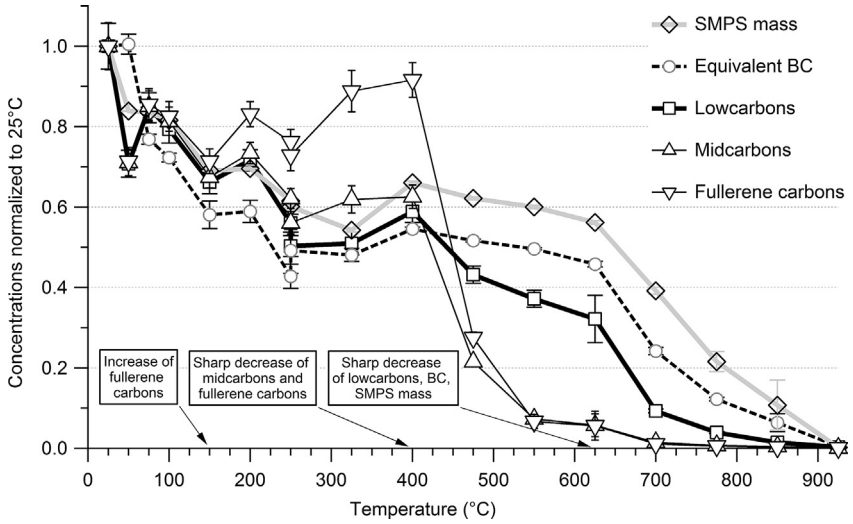

Fig. 9. Soot evaporation and oxidation experiment. SMPS mass estimations (using effective densities from non-heated samples), equivalent BC (aethalometer), and SP-AMS concentrations of low-, mid-, and fullerene-carbons normalized to their concentrations at room temperature (25 °C, the starting point) during temperature ramping of miniCAST OP5 soot (raw exhaust, low oxygen content) from 25 °C–925 °C in a thermodenuder (25 °C–250 °C) and ceramic furnace (250 °C–925 °C).

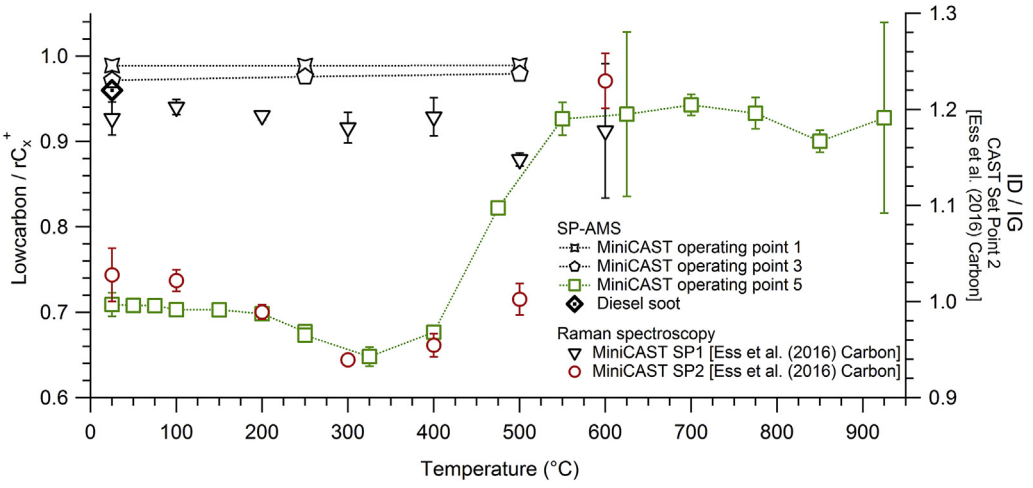

Fig. 10. Lowcarbon ($C_{\leq 5}^+$) to rC_x^+ ratios (left axis) for: miniCAST OP5 soot during temperature ramping from 25 °C to 925 °C; miniCAST OP1 and OP3 soot at 25 °C, 250 °C, and 500 °C; diesel exhaust soot at 25 °C (untreated). The lowcarbon to rC_x^+ ratio is the complement to the large carbons ($C_{\geq 6}^+$) to rC_x^+ ratio. Right axis, Raman spectroscopy analysis of the D and G band intensity ratios (ID/IG) of setpoint 1 and 2 (SP1 and SP2) soot from Ess et al. [79]. (A colour version of this figure can be viewed online.)

carbon nanostructure and suggested to be proportional to fringe length [80,81]. In order to produce soot with higher OC content, Ess et al. [79] reduced only the oxidation air flow of the miniCAST (no N_2 was added). Thus, their "set point" and our "operating point" values represent different miniCAST conditions.

On the right axis, Fig. 10 shows the results from Ess et al. [79] of the ID/IG ratio for soot from set point 1 and 2 during a temperature ramp from 25 °C to 600 °C. For set point 1 soot, they observed an ID/IG ratio close to 1.2 and negligible changes upon temperature ramping. For set point 2 (shown) and set point 3 (not shown) soot, they instead observed a small but significant decrease in the ID/IG ratio from heating up to 300 °C, indicating a decreasing structural order of the soot nanostructure. Further heating (300 °C – 600 °C) strongly increased the ID/IG ratio up to ~1.2 and was interpreted as an ordering of the nanostructure [79].

On the left axis, Fig. 10 shows the lowcarbon to rC_x^+ ratio for miniCAST soot from OP 1, 3, and 5, as well as for diesel soot sampled from an experimental heavy duty engine [53]. Diesel soot and the mature miniCAST soot at OP 1 and 3 had high lowcarbon to rC_x^+ ratios (>0.95) which were not influenced by heating to 500 °C. For soot from OP5, the lowcarbon to rC_x^+ ratio was constant between 25 °C – 150 °C but showed a slight decrease upon heating between 150 °C – 325 °C. Heating above 400 °C sharply increased the lowcarbon to rC_x^+ ratio, from 0.65 at 325 °C to 0.93 at 550 °C. The ratio remained nearly constant and above 0.9 upon further heating from 550 °C to 925 °C.

The increase of large carbons between 150 °C to 325 °C for soot from OP5 occurred at similar temperatures as the decrease in ID/IG ratio for soot from set point 2 [79]. Similarly, the sharp increase in lowcarbon to rC_x^+ ratio between 400 °C – 550 °C coincided with the sharp increase in ID/IG ratio of the set point 2 soot. The similarities between the SP-AMS rC_x^+ analysis and Raman spectroscopy ID/IG analysis provide further evidence for a strong relationship between SP-AMS rC_x^+ distributions and the soot nanostructure. The increase in fullerene carbons from heating of the soot between 150 °C – 325 °C thus appears related to a partial restructuring to less ordered carbon nanostructures, or the formation of such structures from charring of OA. Consequently, we have interpreted the sharp decay of large carbons at 400 °C as related to the oxidation (removal) of particle components associated with the SP-AMS large carbon clusters, and increased graphitization of the carbon nanostructure.

4. Conclusions

This study explored relationships between refractory carbon cluster (rC_x^+) distributions in SP-AMS mass spectra, soot carbon nanostructure, and thermal/oxidation properties of soot components. A linear correlation was found between the SP-AMS large carbon to rC_x^+ ratio and decreasing average fringe length ($r = -0.97$, $p = 0.028$). The comparison between the thermal-optical carbon analysis and the SP-AMS rC_x^+ mass spectra indicated that lowcarbons derive from EC components while large carbons (mid- and fullerene carbons) originated from refractory organic carbon components classified as $OC_{3\text{-}4}$ and components undergoing pyrolysis as OC evolves in the thermal-optical carbon analyzer (i.e., PC). Material related to large carbon ions exhibited different oxidation behavior than that related to lowcarbons and equivalent BC. At temperatures ~200 °C lower than the oxidation of lowcarbons and equivalent BC, the large carbon clusters ($C_{\geq 6}^+$) were no longer detected in SP-AMS mass spectra. Therefore, large carbons (both midcarbons and fullerene carbons) most likely represent particle components chemically separated from and with optical properties different from BC.

In addition to C_6 rings also found in graphitic carbon, fullerenes incorporate C_5 rings. Soot with high tortuosity (curved lamellae) and more reactive nanostructures have been hypothesized to form by partial oxidation of benzene and C_5 chemistry in flames [18,26]. The large carbons in SP-AMS mass spectra may thus provide information on refractory soot composition and nanostructures related to soot reactivity. In modern diesel engines, soot forms in large amounts shortly after ignition and is oxidized in the late combustion cycle. As a result, only a small fraction of the soot initially formed in the combustion exits the engine into the tailpipe [53,82,83]. Identifying soot components which are easily oxidized (removed) may therefore aid in developing new soot mitigation strategies for internal combustion engines. Absorption Angstrom exponents were previously reported to increase with higher miniCAST OP [35]. This suggests that soot particle components responsible for SP-AMS large carbons can have absorption spectra more similar to brown carbon (with absorption Angstrom exponents >>1).

This study also identifies major uncertainties related to the characterization of mass and composition for immature soots. We

may conclude that for the low temperature combustion conditions and immature soots sampled in this study, including only equivalent BC (or EC) and non-refractory OA_{AMS} (conventional AMS measurement, laser off) significantly underestimated the total particulate carbon mass. The additional carbon mass consisted of refractory organic carbon components correlated to large carbons in the SP-AMS (laser on) mass spectra. The incapacity to evaporate the refractory organic carbon material at 500 °C in the furnace, the persistent large carbons in SP-AMS mass spectra, and the stability of the soot nanostructures under the electron beam during HRTEM, suggest that these refractory organic carbon components were constituents incorporated into and part of the internal soot carbon nanostructure (see also e.g., [47]). This may challenge atmospheric BC and OA internal mixing state models assuming stratified particles consisting of a BC core and a coating of condensed low volatility organics (e.g., [48,84]). It also suggests that relationships between equivalent BC to non-refractory OA ratios and the absorptivity of OA may be biased if refractory organic components are present in the soot. SP-AMS large carbons have been observed in soot mass spectra from a number of combustion sources including biomass combustion and in low temperature diesel combustion [51,52,54,55,85]. We therefore suggest a need to reevaluate the internal mixing state model (BC core and organic coating) for soot emissions from such combustion appliances, especially in relation to the underlying causes of increased absorption Angstrom exponents and toxicity.

The results in this study form a basis for interpreting large carbons ($C^+_{\geq 6}$) in aerosol mass spectra from soot and BC-containing materials. This interpretation can aid the design of novel on-line investigations related to refractory organic carbon and C_5-containing structures in engineered carbon nanomaterials and particulate emissions from low temperature combustion. Moreover, it can aid in deciphering the optical, cloud forming, and health relevant properties of such components in ambient soot. Future studies should identify suitable calibrants and develop a mass calibration procedure for SP-AMS large carbons, as well as improve the accuracy with which rC^+_x analysis can provide information on variations in the soot nanostructure.

Acknowledgements

The authors gratefully acknowledge the financial support from The Swedish Research Council FORMAS (research grant 2013-453), The Swedish Research Council VR (research grant 2013-5021), and NanoLund at Lund University (p08-2014). Part of the HRTEM work was conducted under and financed by the Danish Center for Nanosafety. We acknowledge technical support by Dr. Jens Kling (Technical University of Denmark), and Dr. Natalia Ivleva (Technical University of Munich) for sharing Raman spectroscopy data.

Appendix A. Supplementary data

Supplementary data to this article can be found online at https://doi.org/10.1016/j.carbon.2018.10.072.

References

[1] P. Parent, C. Laffon, I. Marhaba, D. Ferry, T.Z. Regier, I.K. Ortega, et al., Nanoscale characterization of aircraft soot: a high-resolution transmission electron microscopy, Raman spectroscopy, X-ray photoelectron and near-edge X-ray absorption spectroscopy study, Carbon 101 (2016) 86–100.
[2] I.E. Nielsen, A.C. Eriksson, R. Lindgren, J. Martinsson, R. Nyström, E.Z. Nordin, et al., Time-resolved analysis of particle emissions from residential biomass combustion – emissions of refractory black carbon, PAHs and organic tracers, Atmos. Environ. 165 (2017) 179–190.
[3] D.B. Kittelson, Engines and nanoparticles: a review, J. Aerosol Sci. 29 (5) (1998) 575–588.
[4] T.C. Bond, S.J. Doherty, D.W. Fahey, P.M. Forster, T. Berntsen, B.J. DeAngelo, et al., Bounding the role of black carbon in the climate system: a scientific assessment, J. Geophys. Res. Atmos. 118 (11) (2013) 5380–5552.
[5] S. Steiner, C. Bisig, A. Petri-Fink, B. Rothen-Rutishauser, Diesel exhaust: current knowledge of adverse effects and underlying cellular mechanisms, Arch. Toxicol. 90 (2016) 1541–1553.
[6] Z.D. Ristovski, B. Miljevic, N.C. Surawski, L. Morawska, K.M. Fong, F. Goh, et al., Respiratory health effects of diesel particulate matter, Respirology 17 (2) (2012) 201–212.
[7] R.J. Laumbach, H.M. Kipen, Respiratory health effects of air pollution: update on biomass smoke and traffic pollution, J. Allergy Clin. Immunol. 129(1) 3-11.
[8] T. Sigsgaard, B. Forsberg, I. Annesi-Maesano, A. Blomberg, A. Bølling, C. Boman, et al., Health impacts of anthropogenic biomass burning in the developed world, Eur. Respir. J. 46 (6) (2015) 1577–1588. ERJ-01865-2014.
[9] IPCC, Climate Change 2013: the Physical Science Basis. Contribution of Working Group I to the Fifth Assessment Report of the Intergovernmental Panel on Climate Change, Cambridge University Press, Cambridge, United Kingdom and New York, NY, USA, 2013.
[10] P.J. Landrigan, R. Fuller, N.J.R. Acosta, O. Adeyi, R. Arnold, N. Basu, et al., The Lancet Commission on pollution and health, Lancet 391 (10119) (2018) 462–512.
[11] T.C. Bond, R.W. Bergstrom, Light absorption by carbonaceous particles: an investigative review, Aerosol Sci. Technol. 40 (1) (2006) 27–67.
[12] M. Matti Maricq, Chemical characterization of particulate emissions from diesel engines: a review, J. Aerosol Sci. 38 (11) (2007) 1079–1118.
[13] K. Yehliu, R.L. Vander Wal, O. Armas, A.L. Boehman, Impact of fuel formulation on the nanostructure and reactivity of diesel soot, Combust. Flame 159 (12) (2012) 3597–3606.
[14] K. Al-Qurashi, A.L. Boehman, Impact of exhaust gas recirculation (EGR) on the oxidative reactivity of diesel engine soot, Combust. Flame 155 (4) (2008) 675–695.
[15] C. Russo, M. Alfè, J.-N. Rouzaud, F. Stanzione, A. Tregrossi, A. Ciajolo, Probing structures of soot formed in premixed flames of methane, ethylene and benzene, Proc. Combust. Inst. 34 (1) (2013) 1885–1892.
[16] L. Wang, C. Song, J. Song, G. Lv, H. Pang, W. Zhang, Aliphatic C–H and oxygenated surface functional groups of diesel in-cylinder soot: characterizations and impact on soot oxidation behavior, Proc. Combust. Inst. 34 (2) (2013) 3099–3106.
[17] H. Wang, Formation of nascent soot and other condensed-phase materials in flames, Proc. Combust. Inst. 33 (1) (2011) 41–67.
[18] C.-H. Huang, R.L. Vander Wal, Partial premixing effects upon soot nanostructure, Combust. Flame 168 (2016) 403–408.
[19] W.J. Grieco, A.L. Lafleur, K.C. Swallow, H. Richter, K. Taghizadeh, J.B. Howard, Fullerenes and PAH in low-pressure premixed benzene/oxygen flames, Symposium (International) on Combustion 27 (2) (1998) 1669–1675.
[20] W.J. Grieco, J.B. Howard, L.C. Rainey, J.B. Vander Sande, Fullerenic carbon in combustion-generated soot, Carbon 38 (4) (2000) 597–614.
[21] A. Goel, P. Hebgen, J.B. Vander Sande, J.B. Howard, Combustion synthesis of fullerenes and fullerenic nanostructures, Carbon 40 (2) (2002) 177–182.
[22] C.K. Gaddam, R.L. Vander Wal, X. Chen, A. Yezerets, K. Kamasamudram, Reconciliation of carbon oxidation rates and activation energies based on changing nanostructure, Carbon 98 (2016) 545–556.
[23] B. Rohani, C. Bae, Morphology and nano-structure of soot in diesel spray and in engine exhaust, Fuel 203 (2017) 47–56.
[24] Y. Ying, D. Liu, Effects of butanol isomers additions on soot nanostructure and reactivity in normal and inverse ethylene diffusion flames, Fuel 205 (2017) 109–129.
[25] R.L. Vander Wal, A.J. Tomasek, Soot nanostructure: dependence upon synthesis conditions, Combust. Flame 136 (1) (2004) 129–140.
[26] R.L. Vander Wal, A. Strzelec, T.J. Toops, C. Stuart Daw, C.L. Genzale, Forensics of soot: C5-related nanostructure as a diagnostic of in-cylinder chemistry, Fuel 113 (2013) 522–526.
[27] D.R. Tree, K.I. Svensson, Soot processes in compression ignition engines, Prog. Energy Combust. Sci. 33 (3) (2007) 272–309.
[28] G. De Falco, M. Sirignano, M. Commodo, L. Merotto, F. Migliorini, R. Dondè, et al., Experimental and numerical study of soot formation and evolution in co-flow laminar partially premixed flames, Fuel 220 (2018) 396–402.
[29] M.L. Botero, D. Chen, S. González-Calera, D. Jefferson, M. Kraft, HRTEM evaluation of soot particles produced by the non-premixed combustion of liquid fuels, Carbon 96 (2016) 459–473.
[30] B. Apicella, P. Pré, M. Alfè, A. Ciajolo, V. Gargiulo, C. Russo, et al., Soot nanostructure evolution in premixed flames by high resolution electron transmission microscopy (HRTEM), Proc. Combust. Inst. 35 (2) (2015) 1895–1902.
[31] M.R. Kholghy, A. Veshkini, M.J. Thomson, The core–shell internal nanostructure of soot – a criterion to model soot maturity, Carbon 100 (2016) 508–536.
[32] R.H. Hurt, G.P. Crawford, H.-S. Shim, Equilibrium nanostructure of primary soot particles, Proc. Combust. Inst. 28 (2) (2000) 2539–2546.
[33] R.L. Vander Wal, A.J. Tomasek, Soot oxidation: dependence upon initial nanostructure, Combust. Flame 134 (1) (2003) 1–9.
[34] X. López-Yglesias, P.E. Schrader, H.A. Michelsen, Soot maturity and absorption cross sections, J. Aerosol Sci. 75 (2014) 43–64.
[35] S. Török, V.B. Malmborg, J. Simonsson, A. Eriksson, J. Martinsson, M. Mannazhi, et al., Investigation of the absorption Ångström exponent and its relation to physicochemical properties for mini-CAST soot, Aerosol Sci. Technol. 52 (7)

(2018) 757–767.
[36] H.A. Michelsen, Probing soot formation, chemical and physical evolution, and oxidation: a review of in situ diagnostic techniques and needs, Proc. Combust. Inst. 36 (1) (2017) 717–735.
[37] J. Simonsson, N.-E. Olofsson, S. Török, P.-E. Bengtsson, H. Bladh, Wavelength dependence of extinction in sooting flat premixed flames in the visible and near-infrared regimes, Appl. Phys. B 119 (4) (2015) 657–667.
[38] M. Commodo, G. De Falco, A. Bruno, C. Borriello, P. Minutolo, A. D'Anna, Physicochemical evolution of nascent soot particles in a laminar premixed flame: from nucleation to early growth, Combust. Flame 162 (10) (2015) 3854–3863.
[39] S.A. Skeen, H.A. Michelsen, K.R. Wilson, D.M. Popolan, A. Violi, N. Hansen, Near-threshold photoionization mass spectra of combustion-generated high-molecular-weight soot precursors, J. Aerosol Sci. 58 (2013) 86–102.
[40] M. Frenklach, Reaction mechanism of soot formation in flames, Phys. Chem. Chem. Phys. 4 (11) (2002) 2028–2037.
[41] M. Frenklach, H. Wang, Detailed modeling of soot particle nucleation and growth, Symposium (International) on Combustion 23 (1) (1991) 1559–1566.
[42] M. Schenk, N. Hansen, H. Vieker, A. Beyer, A. Gölzhäuser, K. Kohse-Höinghaus, PAH formation and soot morphology in flames of C4 fuels, Proc. Combust. Inst. 35 (2) (2015) 1761–1769.
[43] T.S. Totton, D. Chakrabarti, A.J. Misquitta, M. Sander, D.J. Wales, M. Kraft, Modelling the internal structure of nascent soot particles, Combust. Flame 157 (5) (2010) 909–914.
[44] P.T.A. Reilly, R.A. Gieray, W.B. Whitten, J.M. Ramsey, Fullerene evolution in flame-generated soot, J. Am. Chem. Soc. 122 (47) (2000) 11596–11601.
[45] M. Pontier Johnson, J.B. Donnet, T.K. Wang, C.C. Wang, R.W. Locke, B.E. Brinson, et al., A dynamic continuum of nanostructured carbons in the combustion furnace, Carbon 40 (2) (2002) 189–194.
[46] K.O. Johansson, M.P. Head-Gordon, P.E. Schrader, K.R. Wilson, H.A. Michelsen, Resonance-stabilized hydrocarbon-radical chain reactions may explain soot inception and growth, Science 361 (6406) (2018) 997.
[47] M.M. Maricq, Examining the relationship between black carbon and soot in flames and engine exhaust, Aerosol Sci. Technol. 48 (6) (2014) 620–629.
[48] R. Saleh, E.S. Robinson, D.S. Tkacik, A.T. Ahern, S. Liu, A.C. Aiken, et al., Brownness of organics in aerosols from biomass burning linked to their black carbon content, Nat. Geosci. 7 (2014) 647–650.
[49] K. Adachi, A.J. Sedlacek, L. Kleinman, D. Chand, J.M. Hubbe, P.R. Buseck, Volume changes upon heating of aerosol particles from biomass burning using transmission electron microscopy, Aerosol Sci. Technol. 52 (1) (2018) 46–56.
[50] C. Russo, B. Apicella, J.S. Lighty, A. Ciajolo, A. Tregrossi, Optical properties of organic carbon and soot produced in an inverse diffusion flame, Carbon 124 (2017) 372–379.
[51] T.B. Onasch, A. Trimborn, E.C. Fortner, J.T. Jayne, G.L. Kok, L.R. Williams, et al., Soot particle aerosol mass spectrometer: development, validation, and initial application, Aerosol Sci. Technol. 46 (7) (2012) 804–817.
[52] T.B. Onasch, E.C. Fortner, A.M. Trimborn, A.T. Lambe, A.J. Tiwari, L.C. Marr, et al., Investigations of SP-AMS carbon ion distributions as a function of refractory black carbon particle type, Aerosol Sci. Technol. 49 (6) (2015) 409–422.
[53] V.B. Malmborg, A.C. Eriksson, M. Shen, P. Nilsson, Y. Gallo, B. Waldheim, et al., Evolution of in-cylinder diesel engine soot and emission characteristics investigated with on-line aerosol mass spectrometry, Environ. Sci. Technol. 51 (2017) 1876–1885.
[54] J. Corbin, B. Sierau, M. Gysel, M. Laborde, A. Keller, J. Kim, et al., Mass spectrometry of refractory black carbon particles from six sources: carbon-cluster and oxygenated ions, Atmos. Chem. Phys. 14 (5) (2014) 2591–2603.
[55] J. Wang, T.B. Onasch, X. Ge, S. Collier, Q. Zhang, Y. Sun, et al., Observation of fullerene soot in eastern China, Environ. Sci. Technol. Lett. 3 (4) (2016) 121–126.
[56] M.T. Bowers, Ion mobility spectrometry: a personal view of its development at UCSB, Int. J. Mass Spectrom. 370 (2014) 75–95.
[57] R.L. Vander Wal, M.Y. Choi, Pulsed laser heating of soot: morphological changes, Carbon 37 (2) (1999) 231–239.
[58] J.P. Abrahamson, M. Singh, J.P. Mathews, R.L. Vander Wal, Pulsed laser annealing of carbon black, Carbon 124 (2017) 380–390.
[59] R.L. Vander Wal, A.J. Tomasek, T.M. Ticich, Synthesis, laser processing, and flame purification of nanostructured carbon, Nano Lett. 3 (2) (2003) 223–229.
[60] J.P. Abrahamson, A. Jain, A.C.T. van Duin, R.L. Vander Wal, Carbon structure and the resulting graphitizability upon oxygen evolution, Carbon 135 (2018) 171–179.
[61] F. Cavalli, M. Viana, K.E. Yttri, J. Genberg, J.P. Putaud, Toward a standardised thermal-optical protocol for measuring atmospheric organic and elemental carbon: the EUSAAR protocol, Atmos. Meas. Tech. 3 (1) (2010) 79–89.
[62] M. Sakai, H. Iguma, K. Kondo, T. Aizawa, Nanostructure Analysis of Primary Soot Particles Directly Sampled in Diesel Spray Flame via HRTEM, 2012, 2012-01-1722.
[63] Y. Zhang, R. Zhang, S. Kook, Nanostructure analysis of in-flame soot particles under the influence of jet-jet interactions in a light-duty diesel engine, SAE International Journal of Engines 8 (2015) 2213–2226, 2015-24-2444.
[64] Y. Zhang, D. Kim, L. Rao, R. Zhang, S. Kook, K.S. Kim, et al., The soot particle formation process inside the piston bowl of a small-bore diesel engine, Combust. Flame 185 (2017) 278–291.
[65] Y. Zhang, R. Zhang, L. Rao, D. Kim, S. Kook, The influence of a large methyl ester on in-flame soot particle structures in a small-bore diesel engine, Fuel 194 (2017) 423–435.
[66] Y. Zhang, R. Zhang, L. Rao, S. Kook, A Comparison between In-flame and Exhaust Soot Nanostructures in a Light-duty Diesel Engine, 2017, 2017-01-0710.
[67] P.F. DeCarlo, J.R. Kimmel, A. Trimborn, M.J. Northway, J.T. Jayne, A.C. Aiken, et al., Field-deployable, high-resolution, time-of-flight aerosol mass spectrometer, Anal. Chem. 78 (24) (2006) 8281–8289.
[68] W. Xu, A. Lambe, P. Silva, W. Hu, T. Onasch, L. Williams, et al., Laboratory evaluation of species-dependent relative ionization efficiencies in the Aerodyne Aerosol Mass Spectrometer, Aerosol Sci. Technol. (2018) 1–16.
[69] S. Tomita, J.U. Andersen, C. Gottrup, P. Hvelplund, U.V. Pedersen, Dissociation energy for C(2) loss from fullerene cations in a storage ring, Phys. Rev. Lett. 87 (7) (2001), 073401.
[70] S. Tomita, J.U. Andersen, K. Hansen, P. Hvelplund, Stability of buckminsterfullerene, C60, Chem. Phys. Lett. 382 (1) (2003) 120–125.
[71] J. Ma, X. Li, P. Gu, T.R. Dallmann, A.A. Presto, N.M. Donahue, Estimating ambient particulate organic carbon concentrations and partitioning using thermal optical measurements and the volatility basis set, Aerosol Sci. Technol. 50 (6) (2016) 638–651.
[72] F. Drewnick, S.S. Hings, P. DeCarlo, J.T. Jayne, M. Gonin, K. Fuhrer, et al., A new time-of-flight aerosol mass spectrometer (TOF-AMS)—instrument description and first field deployment, Aerosol Sci. Technol. 39 (7) (2005) 637–658.
[73] M.D. Hays, R.L. Vander Wal, Heterogeneous soot nanostructure in atmospheric and combustion source aerosols, Energy Fuels 21 (2) (2007) 801–811.
[74] R.L. Vander Wal, A.J. Tomasek, M.I. Pamphlet, C.D. Taylor, W.K. Thompson, Analysis of HRTEM images for carbon nanostructure quantification, J. Nanoparticle Res. 6 (6) (2004) 555–568.
[75] C. Hu, W. Li, Q. Lin, X. Zheng, H. Pan, Q. Huang, Impact of ferrocene on the nanostructure and functional groups of soot in a propane/oxygen diffusion flame, RSC Adv. 7 (9) (2017) 5427–5436.
[76] X. Li, Z. Xu, C. Guan, Z. Huang, Oxidative reactivity of particles emitted from a diesel engine operating at light load with EGR, Aerosol Sci. Technol. 49 (1) (2015) 1–10.
[77] Z. Li, C. Song, J. Song, G. Lv, S. Dong, Z. Zhao, Evolution of the nanostructure, fractal dimension and size of in-cylinder soot during diesel combustion process, Combust. Flame 158 (8) (2011) 1624–1630.
[78] S.H. Kim, R.A. Fletcher, M.R. Zachariah, Understanding the difference in oxidative properties between flame and diesel soot Nanoparticles: the role of metals, Environ. Sci. Technol. 39 (11) (2005) 4021–4026.
[79] M.N. Ess, D. Ferry, E.D. Kireeva, R. Niessner, F.X. Ouf, N.P. Ivleva, In situ Raman microspectroscopic analysis of soot samples with different organic carbon content: structural changes during heating, Carbon 105 (2016) 572–585.
[80] A.C. Ferrari, J. Robertson, Interpretation of Raman spectra of disordered and amorphous carbon, Phys. Rev. B 61 (20) (2000) 14095–14107.
[81] F. Tuinstra, J.L. Koenig, Raman spectrum of graphite, J. Chem. Phys. 53 (3) (1970) 1126–1130.
[82] Y. Gallo, J. Simonsson, T. Lind, P.-E. Bengtsson, H. Bladh, O. Andersson, A Study of In-cylinder Soot Oxidation by Laser Extinction Measurements during an EGR-sweep in an Optical Diesel Engine, SAE Technical Paper, 2015, 2015–01–0800.
[83] Y. Gallo, V.B. Malmborg, J. Simonsson, E. Svensson, M. Shen, P.-E. Bengtsson, et al., Investigation of late-cycle soot oxidation using laser extinction and in-cylinder gas sampling at varying inlet oxygen concentrations in diesel engines, Fuel 193 (2017) 308–314.
[84] D.A. Lack, J.M. Langridge, R. Bahreini, C.D. Cappa, A.M. Middlebrook, J.P. Schwarz, Brown carbon and internal mixing in biomass burning particles, Proc. Natl. Acad. Sci. U. S. A. 109 (37) (2012) 14802–14807.
[85] E. Fortner, T. Onasch, M. Canagaratna, L.R. Williams, T. Lee, J. Jayne, et al., Examining the chemical composition of black carbon particles from biomass burning with SP-AMS, J. Aerosol Sci. 120 (2018) 12–21.